2020

Lanthanide-doped lanthanum hafnate nanoparticles as multicolor phosphors for warm white lighting and scintillators

Santosh K. Gupta
The University of Texas Rio Grande Valley

Jose P. Zuniga
The University of Texas Rio Grande Valley

Maya Abdou
The University of Texas Rio Grande Valley

Melonie P. Thomas
The University of Texas Rio Grande Valley

Manisha De Alwis Goonatilleke

See next page for additional authors

Chemical Engineering Journal 379 (2020) 122314

Contents lists available at ScienceDirect

Chemical Engineering Journal

journal homepage: www.elsevier.com/locate/cej

Lanthanide-doped lanthanum hafnate nanoparticles as multicolor phosphors for warm white lighting and scintillators

Santosh K. Gupta[a,b], Jose P. Zuniga[a], Maya Abdou[a], Melonie P. Thomas[c], Manisha De Alwis Goonatilleke[c], Beth S. Guiton[c], Yuanbing Mao[a,d,*]

[a] Department of Chemistry, University of Texas Rio Grande Valley, 1201 West University Drive, Edinburg, TX 78539, USA
[b] Radiochemistry Division, Bhabha Atomic Research Centre, Trombay, Mumbai 400085, India
[c] Department of Chemistry, University of Kentucky, 505 Rose Street, Lexington, KY 40506, USA
[d] School of Earth, Environmental, and Marine Sciences, University of Texas Rio Grande Valley, 1201 West University Drive, Edinburg, TX 78539, USA

HIGHLIGHTS

- Facile and low temperature molten-salt synthesis.
- Multicolor photo and radioluminescent phosphor.
- Distinct Concentration quenching for different lanthanide dopant.
- Eu/Dy distributed at La^{3+} and Hf^{4+} site whereas Tb^{3+} ions are localized only at Hf^{4+} site.
- Warm white light is achieve by engineering the dopant ions and their concentration.

GRAPHICAL ABSTRACT

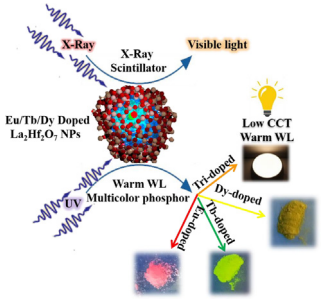

ARTICLE INFO

Keywords:
Lanthanum hafnate
Pyrochlore
Luminescence
Warm white light
Scintillation

ABSTRACT

Designing luminescent materials especially nanomaterials with multifunctional applications is highly challenging and demanding. In this work, we explored pyrochlore $La_2Hf_2O_7$ nanoparticles (NPs) singly and triply co-doped with Eu^{3+}, Tb^{3+} and Dy^{3+}. Under both ultraviolet and X-ray irradiations, the $La_2Hf_2O_7$ NPs singly doped with Eu^{3+}, Tb^{3+} and Dy^{3+} displayed red, green and yellowish-blue emission, respectively. The concentration quenching study revealed a non-radiative energy transfer in Eu^{3+} doped $La_2Hf_2O_7$ NPs, which takes place via dipole-quadrupole mechanism. On the other hand, a dipole-dipole interaction prevails in Tb^{3+} and Dy^{3+} doped $La_2Hf_2O_7$ NPs. Lifetime spectroscopy reveals the stabilization of Eu^{3+} and Dy^{3+} ions at La^{3+} site at low doping concentration whereas a fraction of them migrates to Hf^{4+} site at high doping concentration. For the $La_2Hf_2O_7$:Tb^{3+} NPs, Tb^{3+} ions are localized at Hf^{4+} site at all doping concentrations. Furthermore, when triply codoped with Eu^{3+}, Tb^{3+} and Dy^{3+} ions, the $La_2Hf_2O_7$ NPs display beautiful warm white light as a new strategy for color tunability through doping percentage. To sum, our complete spectrum of studies on the structure, UV excited photoluminescence, concentration quenching, and local site spectroscopy of the $La_2Hf_2O_7$:Ln^{3+} NPs suggests that they are potential candidates as single-component multicolor-emitting phosphors for lighting and scintillating applications.

* Corresponding author at: Department of Chemistry, University of Texas Rio Grande Valley, 1201 West University Drive, Edinburg, TX 78539, USA.
E-mail address: yuanbing.mao@utrgv.edu (Y. Mao).

https://doi.org/10.1016/j.cej.2019.122314
Received 9 May 2019; Received in revised form 19 July 2019; Accepted 20 July 2019
Available online 22 July 2019
1385-8947/

1. Introduction

Due to the low efficiency, environmental concerns and high cost associated with conventional incandescent bulb and fluorescent lamp, phosphor converting light emitting diodes (pcLEDs) have been in high demand to replace the traditional lamps [1]. As a result, there has been an upsurge of research activities on design and development of new luminescent materials with high color purity, high quantum efficiency and good thermal stability for various applications such as automobile industry, liquid crystal display, horticultural, or solid state lighting [2–4].

Current white light LEDs have a combination of a yellow emitting YAG:Ce phosphor and a blue emitting LED (InGaN) with high chemical and thermal stability. For white light or colored phosphors, the simultaneous generation of red, green and blue (RGB) is necessary [5]. Based on RGB analogy, characteristic emission from rare-earth ions can be combined to design white light phosphors for solid-state lighting which has several advantages such as long lifetimes, lower-energy consumption, high luminous efficiency and environmentally friendly characteristics [5–8]. Due to the lack of red component (CRI < 75), their applicability is more restricted to cool white light which is suited for outdoor applications, i.e. automobile headlight [1,9]. Therefore, there has been growing interest among luminescence material scientists for designing warm white light phosphors for indoor and office lighting applications [10,11]. Warm white light LEDs with low correlated color temperature (CCT) (CCT ≤ 3500 K) are highly recommended for human eyesight [10,11]. To the best of our knowledge, there is no report in literature exploiting pyrochlore hosts for warm white lighting with low CCT. In most of the reports, researchers have seldomly adquired warm white light with low CCT for indoor lighting applications [11–13]. This limitation causes the problem of glare in the eyes which is not good for the retina. Therefore, it becomes imperative to develop single-phased warm white light emitting phosphors with low CCT.

Oxides have been widely explored as phosphor and luminescence hosts due to their wide band gap, ease of synthesis, easy to handle, and high structural and thermal stability. This fact also clearly reflects in their commercial viability in various phosphors such as a YAG:Ce [1,9], Y_2O_3:Eu [14], Y_2O_2S:Eu [15], $LaPO_4$:Ce,Tb [16]. Among oxide hosts, lanthanum hafnate, $La_2Hf_2O_7$, has barely been explored as a phosphor host for white light LEDs [17–22]. Also, it provides high stopping power for X- and γ-rays due to its high density of 7.9 g/cm^3 and the presence of Hf with Z = 72 [23,24]. $La_2Hf_2O_7$ exists in just one crystal structure - cubic pyrochlore, space group Fd-3 m and a = 10.785 Å [25]. With such properties, lanthanum hafnate is considered a potentially good matrix for novel high energy radiation detectors - scintillators and X-ray phosphors. Initially, when highly energetic X-ray beam falls on the pyrochlore $La_2Hf_2O_7$ NPs, it interacts with the hafnium atom (high Z) of the pyrochlore lattice (high density) mainly via the photoelectric effect. This photoelectric interaction generates large quantity of electrons and holes, making an electronic transport to occur between the pyrochlore $La_2Hf_2O_7$ NPs. The hot electrons and holes are then thermalized quickly at the CB and VB edges of the pyrochlore. The electrons in the CB decay non-radiatively to the bottom of the CB and then recombine with holes created in the VB. The e^--h^+ recombination energy released can be used to excite Ln^{3+} ions leading to the characteristics of Ln^{3+} emissions. The trapping and radiative recombination of e^--h^+ pairs can be precisely controlled, which can be used to create tunable luminescence by altering the band gap of materials.

X-ray luminescence optical imaging has been recognized as a powerful technique for medical diagnosis due to its deep penetration and low auto-fluorescence in tissues. With regard to the potential applications in bioimaging, the light output of the nanophosphors under X-ray irradiation is a very important characteristic. In the past, the spectroscopic investigation of $La_2Hf_2O_7$ doped with ions such as Eu^{3+}, Tb^{3+}, Pr^{3+} or Ce^{3+} proved that the matrix is able to transfer the gained energy to dopants and produce luminescence with significant intensity [23,24,26–29]. Each of the lanthanide ions has characteristic emission depending upon the energy level diagram. The most prominent visible emitting lanthanide ions are Dy^{3+} in blue-yellow region, Eu^{3+}/Sm^{3+} in orange-red and Tb^{3+} in green region [30]. White light emission in a single component phosphor using triply co-doped rare earth ions is reported in Eu,Tb,Dy co-doped borate and Eu,Dy,Tm co-doped tungstate based compounds which exhibited excellent performance [31,32]. To the best of our knowledge, luminescence study of individually doped LHO by Dy^{3+} ion and tri-doped $La_2Hf_2O_7$:Tb^{3+}, Eu^{3+},Dy^{3+} has not been reported. In addition, there is absolutely no report on the radioluminescence studies of Dy^{3+} and Tb^{3+} doped $La_2Hf_2O_7$ for potential green and near white X-ray phosphors.

Furthermore, rare earth doped oxide nanoparticles for photonics application have several advantages such as resistance to photobleaching/photoblinking, high color purity, narrow emission, large stokes shifts, etc [33]. In addition, their emission wavelengths do not change much because equilibrium geometry of the ground state and excited state wavefunction is the same. These properties make them excellent candidate for solid-state lighting and light emitting displays. Moreover, materials with $A_2B_2O_7$ pyrochlore composition recently have displayed a variety of advanced applications in solid oxide fuel cells [34,35], photocatalysis [36,37], thermographic phosphor [38], thermal barrier coatings [39], X-ray scintillator [23,24], photoluminescence [40], and nuclear waste host [41], etc. because of their interesting thermo-, physio- and chemical properties.

Compared to microcrystalline phosphors, nanoparticles are expected to offer several advantages, such as easy surface modification, tunable luminescence, superior bioimaging and coating performance, higher electron-hole overlap integral, etc [42]. For white LED devices, it is easier to cast nanoparticle powders into films as an important requirement for commercial applications. Moreover, property tunability is also easier to achieve for nanocrystalline powder compared to microcrystalline counterpart for white light phosphors in case of color coordinate and color temperature, etc [42]. Also, non-uniform microcrystalline phosphor powder has poor adhesion to substrates and would lose contact with LED substrates and enclosures [43]. In addition, the conventional solid-state reaction route for synthesizing normal microcrystalline powder requires temperatures in excess of 1,400 K and suffer from inhomogeneous and coarse particle formation with non-uniform size distribution. For good luminescence characteristics, phosphors must have fine size, narrow size distribution, no aggregation, and spherical morphology. Similarly, several disadvantages have also been noted for some other synthetic techniques, such as the evaporation of solvents resulting in phase segregation, alteration of the stoichiometry due to incomplete precipitation, expensive chemicals, and time-consuming processes. Moreover, nanoparticles are preferable for radioluminescence due to their high surface-to-volume ratio (S/V) which imparts efficient surface loading and multivalent binding to facilitate specificity [44].

To meet the challenges of multicolor NUV and X-ray phosphors for warm white lighting and scintillating applications, in this paper, we have proposed a simple, low temperature molten salt synthesis (MSS) approach to develop lanthanide-doped $La_2Hf_2O_7$ pyrochlore phosphors. Once being excited with 265 nm UV light, singly doped $La_2Hf_2O_7$:Tb^{3+} NPs mainly emit green light at 540 nm, $La_2Hf_2O_7$:Eu^{3+} NPs emit red light at 612 and 630 nm, and $La_2Hf_2O_7$:Dy^{3+} NPs emit yellow light at 577 nm and blue light at 478 nm. We report the generation and color tunability of warm white light from triply doped $La_2Hf_2O_7$:Tb^{3+},Eu^{3+},Dy^{3+} NPs for the production of warm white LEDs with an effective absorption in the ultraviolet window range. Moreover, we studied their optical performance under X-ray irradiation. These X-ray phosphors are expected to display high absorption cross section for X-ray and intense radioluminescence (RL) in the visible spectrum. Compared to bulk scintillator, these pyrochlore NPs can exhibit tunable RL across the visible wavelengths by tailoring the dopant ions.

2. Experimental

2.1. Synthesis

Commercially available lanthanum nitrate hexahydrate ($La(NO_3)_3{\cdot}6H_2O$, 99.0%), hafnium dichloride oxide octahydrate ($HfCl_2O{\cdot}8H_2O$, 98%), europium nitrate pentahydrate ($Eu(NO_3)_3{\cdot}5H_2O$, 99.9%), dysprosium (III) nitrate hydrate ($Dy(NO_3)_3{\cdot}xH_2O$, 99.9%), terbium(III) nitrate pentahydrate ($Tb(NO_3)_3{\cdot}5H_2O$, 99.9%), potassium nitrate (KNO_3, 99.9%), and sodium nitrate ($NaNO_3$, 98%) were used as purchased without further purification. Our synthesis protocol includes a two-step procedure, i.e. coprecipitation process followed by a molten salt synthesis (MSS) [24,45–48]. For the coprecipitation step, stoichiometric amount of starting reactants, i.e. 5 mmol $HfCl_2O{\cdot}8H_2O$, (5-x) mmol $La(NO_3)_3{\cdot}6H_2O$, and x mmol dopant precursor or their mixture, is used. The starting reactants were weighted, dissolved in 200 mL of distilled water (18.2 MΩ at 25 °C), and kept stirring for 30 min. The mixture was then titrated with 200 mL of 10% ammonium hydroxide solution (diluted from commercial 28–30% NH_4OH aqueous solution) over a period of 2 h. The resulting precipitate was then washed with distilled water for several times before being vacuum filtrated and then air dried at room temperature. In the MSS step, the obtained precursor was mixed with potassium nitrate and sodium nitrate in a stoichiometric ratio of (1:30:30) and finely grinded. The resulting mixture was then annealed at 650 °C for 6 h with ramp-up and -down rates of 1°C/min. The final product was washed several times with distilled water and dried in the oven at 90 °C overnight. The singly doped $La_2Hf_2O_7{:}Eu^{3+}$, $La_2Hf_2O_7{:}Tb^{3+}$, and $La_2Hf_2O_7{:}Dy^{3+}$ NPs are designated as LHOE, LHOT and LHOD, respectively.

2.2. Characterization

The structural and morphological characters of the obtained samples were extensively studied using powder X-ray diffraction (XRD), scanning electron microscopy (SEM), and Raman spectroscopy. XRD patterns were recorded using a Rigaku Miniflex X-ray Diffractometer with a Cu $K_{\alpha1}$ radiation (λ = 0.15406 nm, 30 kV and 15 mA) at a 2-theta scanning mode in a scanning range of 10° to 90°. The used scanning step size was 0.05° with a scanning rate of $2°{\cdot}min^{-1}$. Raman spectra were obtained with a Bruker SENTERRA Raman spectrometer (Bruker Optics SENTERRA R200) that uses solid state laser (785 nm) with 100 mW power. A Carl Zeiss sigma VP SEM equipped with a field emission gun operated at 5 kV was used to collect SEM images of the samples.

The actual doping concentration of the NPs (individually doped and triply co-doped) is estimated using energy dispersive spectroscopy (EDS). EDS data were acquired using a FEI Talos F200X TEM system which includes a super-X EDS system with four silicon drift detectors (SDDs) with a solid angle of 0.9 srad. The EDS data was quantified using the Velox software incorporated in the Talos with a standard Cliff-Lorimer (K-factor) method. An absorption correction function was used to correct for the absorption of X-rays by the samples.

Optical properties of the samples were evaluated using time resolved photoluminescence spectroscopy (TRPS), X-ray excited optical luminescence (XEOL), and quantum yield measurements. Photoluminescence (PL) emission, excitation, and lifetime spectra were recorded using an Edinburgh Instrument FLS 980 fluorometer system equipped with a steady state xenon lamp source and a pulsed xenon lamp with a pulse frequency range of 1–100 Hz. A 150 mm BenFlect coated integrating sphere was used to determine the absolute quantum yield (QY) of the NPs. The spectral sensitivity of the spectrometer and the sphere was modified using a calibrated lamp for spectral light throughput. Finally, XEOL spectra were obtained using a silver X-ray source tube with a power of 12 W (60 kV and 200 μA) adapted to the Edinburgh Instruments FLS 980 fluorometer system.

Table 1
Nominal and actual dopant concentrations of the LHOE, LHOT and LHOD NPs.

Sample	Nominal dopant concentrations (mol%)		Actual dopant concentrations (mol %)	
LHOE	**Eu2Hf2O7**	**La2Hf2O7**	**Eu2Hf2O7**	**La2Hf2O7**
	0.5	99.5	0.69	99.31
	1.0	99.0	1.64	98.36
	2.5	97.5	3.53	96.47
	5.0	95.0	5.25	94.75
	7.5	92.5	8.30	91.70
	10.0	90.0	10.21	89.79
LHOT	**$Tb_2Hf_2O_7$**	**$La_2Hf_2O_7$**	**$Tb_2Hf_2O_7$**	**$La_2Hf_2O_7$**
	0.5	99.5	6.98	93.02
	1.0	99.0	6.99	93.01
	2.5	97.5	8.09	91.91
	5.0	95.0	11.59	88.41
	7.5	92.5	15.63	84.37
	10.0	90.0	16.91	83.09
	$Dy_2Hf_2O_7$	**$La_2Hf_2O_7$**	**$Dy_2Hf_2O_7$**	**$La_2Hf_2O_7$**
LHOD	0.5	99.5	0.57	99.43
	1.0	99.0	1.01	98.99
	2.5	97.5	2.00	98.00
	5.0	95.0	4.47	95.53
	7.5	92.5	5.22	94.78
	10.0	90.0	8.65	91.35

3. Results and discussion

3.1. EDS and XRD measurements

The elemental composition analysis by the EDS technique confirms that the actual concentrations of dopant ions in the LHO host are consistent with their nominal ones as tabulated in Table 1.

The powder XRD patterns of the LHOE, LHOT and LHOD NPs (Fig. 1a–c, respectively) can be easily indexed to $La_2Hf_2O_7$ (JCPDS #01-073-0445). There is not much change in lattice parameter for all three series of samples upon increasing the dopant concentration of lanthanide ions (Eu, Tb and Dy) from 0.1 to 10.0 mol% (Table 2) [49]. This is attributed to closeness in ionic size between 8-ccordinated La^{3+} ion (1.16 Å) and that of Eu^{3+} (1.06 Å), Tb^{3+} (1.04 Å) and Dy^{3+} (1.03 Å) ion [50].

Using the Debye-Scherrer equation and based on the [2 2 2] reflection, all the samples have calculated average crystallite size in the range of 17–25 nm. There is systematic decrease of the crystallite size with increasing dopant concentration from 0.5 to 10.0 mol% for all three dopants (Fig. 1d). This is mainly attributed to the distortion of LHO host induced by incorporating dopant ions which can retard the growth of the doped LHO NPs [51].

3.2. Raman spectroscopy

The Raman peaks from the LHOE, LHOT, and LHOD NPs (Fig. 2a–c) are presented at 307, 318, 395, 503, 521, and 609 cm^{-1} corresponding to F_{2g}, E_g, F_{2g}, A_{1g}, F_{2g}, and F_{2g} modes of pyrochlore structure, respectively [24]. Based on group theory, the ideal pyrochlore phase of $A_2B_2O_7$ compounds have six Raman active modes in the range of 200–1000 cm^{-1} with five of them involving M − O vibrations and the one at highest wavenumber related to oxygen sublattice [52,53]. Specifically, the Raman peaks in the wavenumber region of 300–400 cm^{-1} originate from vibrations of the metal–oxygen bonds, i.e. La–O and Hf–O bonds. The peaks at high wavenumbers of 522 and 609 cm^{-1} arise from the stretching of the Hf–O bonds. The Raman band at 394 cm^{-1} is originated from F_{2g} mode due to vibrations from both La-O and Hf-O bonds. The 503 cm^{-1} peak arises from A_{1g} mode due to the bending of -O-Hf-O- bond in HfO_6 octahedra [54]. The small peak around 783 cm^{-1} is ascribed to the distortion of HfO_6 octahedra [55].

The broadening extent of Raman peaks indicates the level of disordering in a sample. The FWHM of the 307 cm^{-1} peak follows the

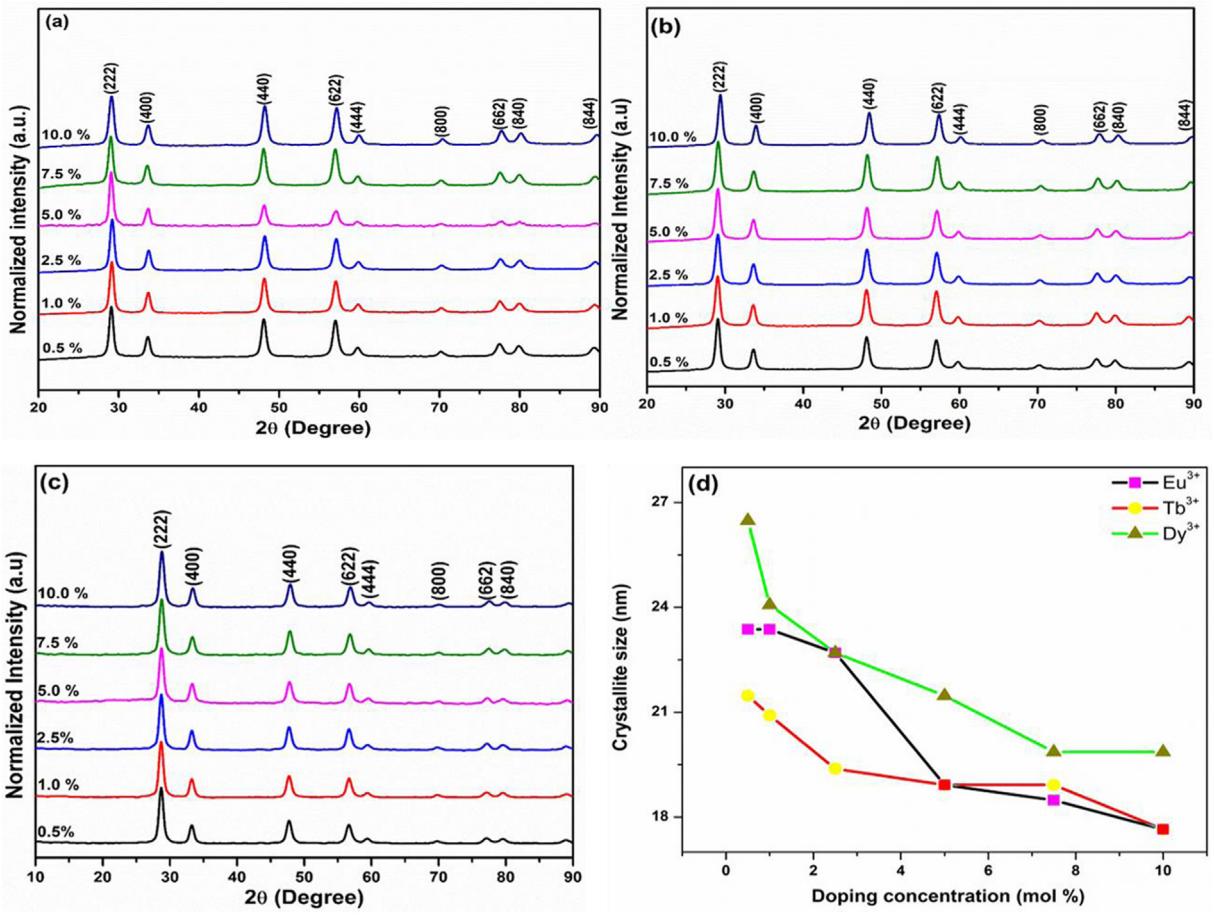

Fig. 1. XRD patterns of the (a) LHOE, (b) LHOT, (c) LHOD NPs. (d) Variation of the crystallite size as a function of dopant concentration of the LHOE, LHOT and LHOD NPs.

Table 2
Calculated lattice parameter and particle size of the LHOE, LHOT and LHOD NPs under various molar doping levels.

x	2θ(°)	FWHM (β)	Lattice parameters (Å)	Crystallite size (nm)
$La_2Hf_2O_7$:*x*%Eu^{3+}				
0.5	29.08	0.34	10.63	23.37
1.0	29.14	0.34	10.61	23.37
2.5	29.19	0.35	10.59	22.70
5.0	28.66	0.43	10.78	18.92
7.5	29.01	0.42	10.65	18.48
10.0	29.12	0.45	10.61	17.65
$La_2Hf_2O_7$:*x*%Tb^{3+}				
0.5	29.07	0.37	10.63	21.47
1.0	29.03	0.38	10.65	20.91
2.5	29.06	0.41	10.64	19.38
5.0	29.06	0.42	10.64	18.92
7.5	29.10	0.42	10.62	18.92
10.0	29.38	0.45	10.52	17.65
$La_2Hf_2O_7$:*x*%Dy^{3+}				
0.5	28.70	0.30	10.77	26.48
1.0	28.69	0.33	10.77	24.07
2.5	28.71	0.35	10.76	22.70
5.0	28.74	0.37	10.75	21.47
7.5	28.77	0.40	10.74	19.86
10.0	28.81	0.40	10.73	19.86

trend of LHOD > LHOT > LHOE. This is possibly related to the difference of ionic radii (Δ*r*) between La^{3+} and the dopant ions, i.e. Δ*r* (La^{3+}-Dy^{3+}) > Δ*r* (La^{3+}-Tb^{3+}) > Δ*r* (La^{3+}-Eu^{3+}).

3.3. SEM

The LHOE, LHOT and LHOD NPs are spherical in morphology with an average size of 36–43 nm which is hardly affected by the identity of dopant ions (Fig. 3). In general, these NPs are highly homogeneous and monodispersed. Spherical NPs are preferable for high brightness due to high packing density and low light scattering [56]. Therefore, our doped LHO NPs are highly desirable as nanophosphors to have desirable luminescent performance.

3.4. PL

3.4.1. Excitation spectra

The excitation spectra of the LHOE NPs (Fig. 4a) show a broad band in the range of 250–315 nm due to O^{2-}→Eu^{3+} charge transfer and fine features in the range of 320–550 nm from the Eu^{3+} intramolecular f-f bands. One interesting feature is the highly intense peaks at 393 and 465 nm due to $^7F_0$→$^5L_6$ and $^7F_0$→$^5D_2$ transitions, respectively, which endow the LHOE NPs as important nanophosphors to be efficiently pumped by NUV at 393 nm and blue light.

The excitation spectra of the LHOT NPs (Fig. 4b) have the three peaks at 220, 285, and 310 nm corresponding to transitions from $^7F_6$ level to the split 5d energy levels of Tb^{3+} ions. The 4d energy levels of Tb^{3+} have both low spin and high spin states designated by ^7D_j and ^9D_j energy levels (J = 0–5), respectively [57]. The most intense peak at 285 nm is attributed to the low spin allowed f–d transition from the $^7F_6$→$^7D_5$. The peaks at 220 and 310 nm are ascribed to the allowed $^7F_6$→$^7D_5$ transition and f–d forbidden high spin $^7F_6$→$^7D_4$ transition, respectively [58].

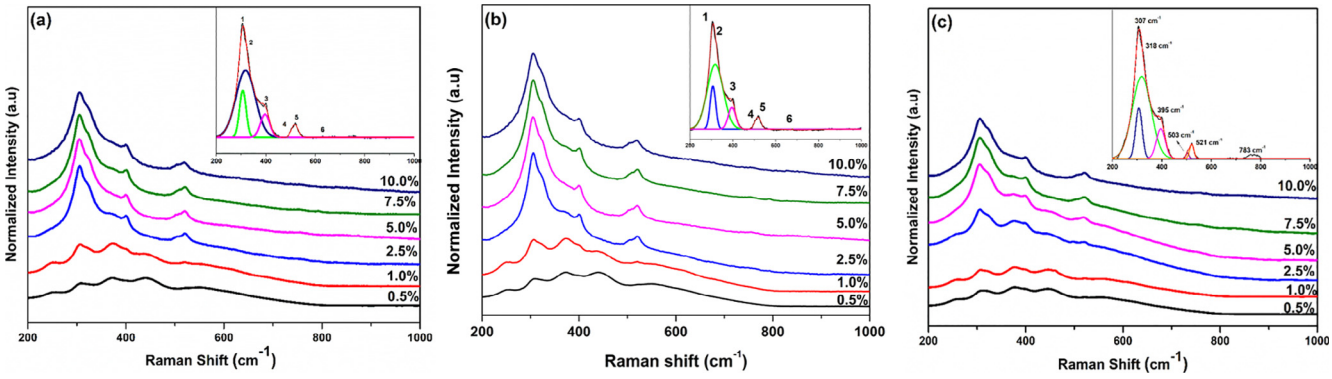

Fig. 2. Raman spectra of the (a) LHOE, (b) LHOT, and (c) LHOD NPs.

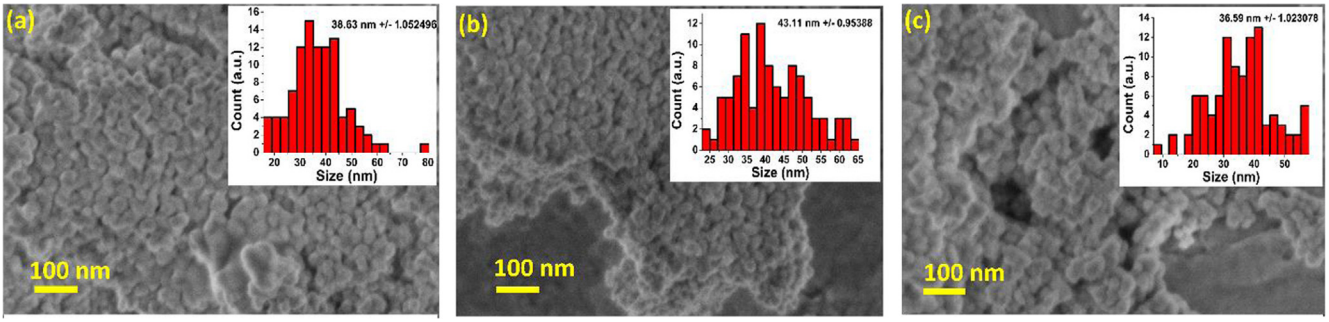

Fig. 3. SEM images of the (a) LHOE, (b) LHOT, and (c) LHOD NPs with 0.5% doping level. The insets are histograms of the estimated particle size using the ImageJ software of 100 particles from the SEM images.

The excitation spectra of the LHOD NPs (Fig. 4c) demonstrate a broad band centered at 258 nm ascribed to the $O^{2-}\rightarrow Dy^{3+}$ charge transfer transition and three intense peaks at 294, 323 and 351 nm due to $^6H_{15/2}\rightarrow{}^4H_{11/2}$ + $^4G_{9/2}$, $^6H_{15/2}\rightarrow{}^4M_{17/2}$, and $^6H_{15/2}\rightarrow{}^6P_{7/2}$ transitions, respectively [59].

3.4.2. Emission spectra

The LHOE NPs (Fig. 5a) show strong emission at 593, 612, 655 and 710 nm corresponding to $^5D_0\rightarrow{}^7F_1$, $^5D_0\rightarrow{}^7F_2$, $^5D_0\rightarrow{}^7F_3$ and $^5D_0\rightarrow{}^7F_4$ transitions of Eu^{3+} ions, respectively. The orange emission band at 593 nm is characterized by the magnetic dipole $^5D_0\rightarrow{}^7F_1$ transition (MDT) of Eu^{3+} and is not affected by the crystal field strength. The red emission peak at 612 nm arises due to the electric dipole $^5D_0\rightarrow{}^7F_2$ transition (EDT) of Eu^{3+}, which is hypersensitive ($\Delta J = \pm 1$) to its local surroundings. Its intensity and splitting strongly depend on the symmetry of the crystal field. The integrated PL intensity ratio of the EDT to MDT known as asymmetry ratio (A_{21}) gives local structure information of Eu^{3+} ions. For the LHOE NPs, the peak at 612 nm is more intense than the peak at 593 nm, which suggests low symmetry around Eu^{3+} in these NPs [24,45,46]. Inset of Fig. 5a shows a digital image of the red emitting LHOE-5.0% NPs.

The LHOT NPs emit at 487, 543, 584, 623, 648, 673 and 688 nm due to the $^5D_4\rightarrow{}^7F_J$ transitions of Tb^{3+} with J = 6, 5, 4, 3, 2, 1 and 0, respectively (Fig. 5b). Similar to the literature, the $^5D_4\rightarrow{}^7F_{0\text{-}1}$ emission peaks are very weak, and the emission intensity generally follows the pattern of $^5D_4\rightarrow{}^7F_6 > {}^5D_4\rightarrow{}^7F_4 > {}^5D_4\rightarrow{}^7F_3 > {}^5D_4\rightarrow{}^7F_2$ [60,61]. Specifically, the green emission band at 543 nm originates from the $^5D_4\rightarrow{}^7F_5$ MDT of Tb^{3+} ions. The blue emission band at 487 nm is due to the $^5D_4\rightarrow{}^7F_6$ EDT of Tb^{3+}, which is affected by local structure and symmetry of Tb^{3+} [62]. The 543 nm band is more intense than the 487 nm band. It can be postulated that a large fraction of Tb^{3+} ions occupy relatively symmetric environment in the LHO host. The presence of both EDT and MDT in the emission spectra of the LHOT NPs suggests that Tb^{3+} ions are distributed at both La^{3+} and Hf^{4+} sites although the

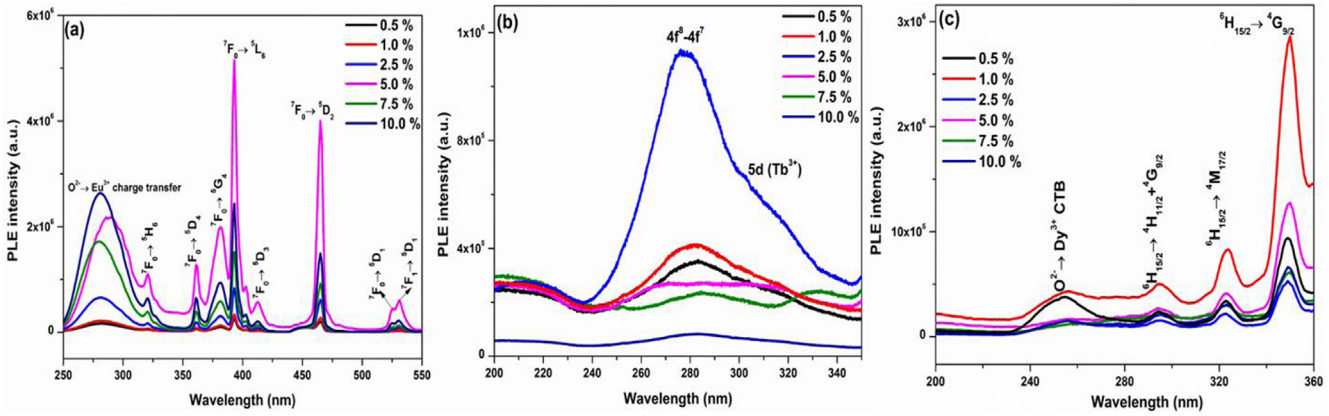

Fig. 4. PL excitation spectra of the (a) LHOE (λ_{em} = 612 nm), (b) LHOT (λ_{em} = 543 nm) and (c) LHOD (λ_{em} = 577 nm) NPs.

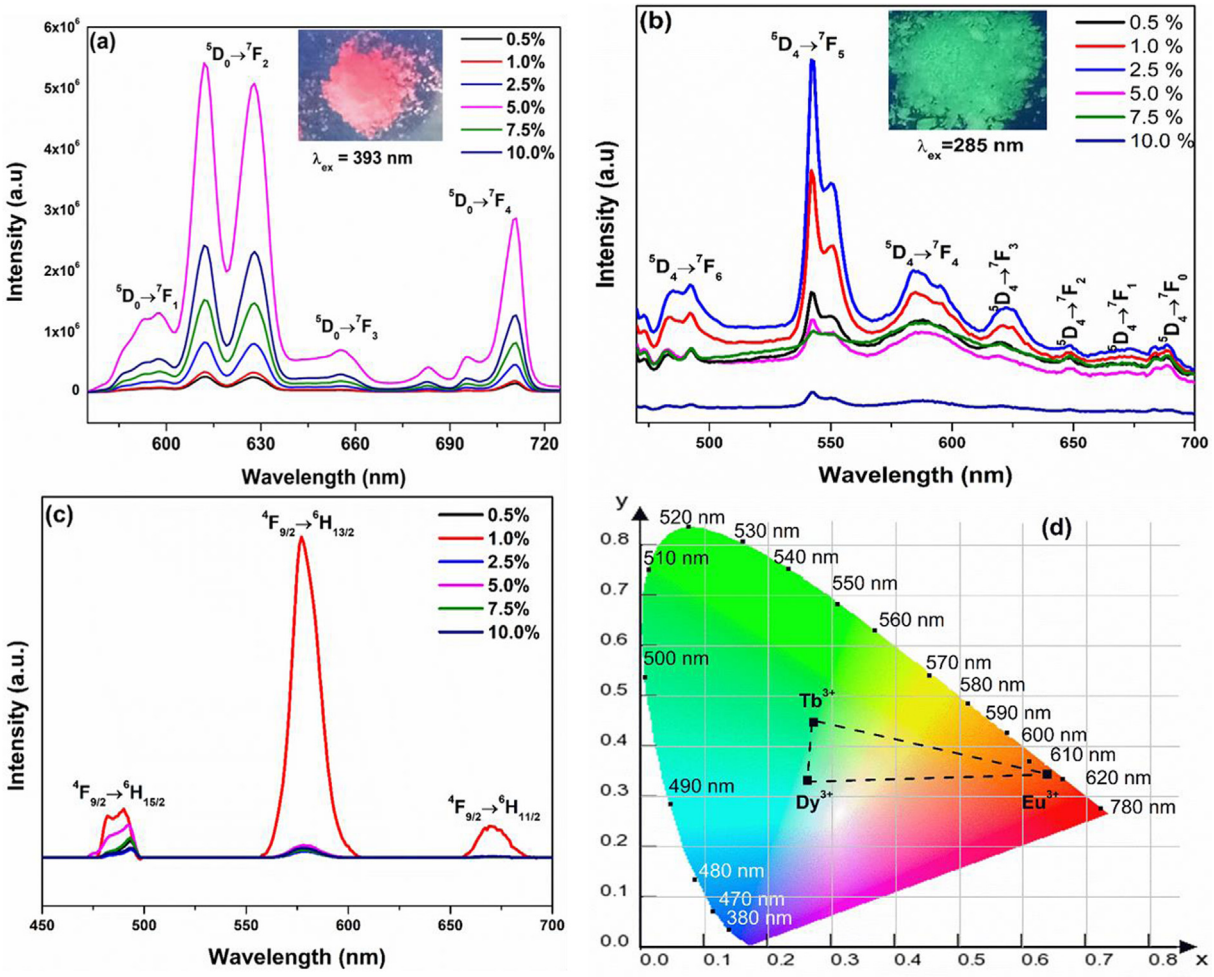

Fig. 5. PL emission spectra of the (a) LHOE (λ_{ex} = 393 nm), (b) LHOT (λ_{ex} = 285 nm), and (c) LHOD (λ_{ex} = 351 nm) NPs. Insets of Fig. 5a and b are the digital images of red and green emissions after NUV lamp excitation of the LHOE-5.0% and LHOT-2.5% NPs, respectively. (d) CIE color coordinate diagram depicting the emission from the LHOE-5.0%, LHOT-2.5%, and LHOD-1.0% NPs.

majority prefers to stabilize at the symmetric HfO_6 octahedra in the LHO host. Inset of Fig. 5b shows a digital image of the green emitting LHOT-5.0% NPs.

The emission spectra of the LHOD NPs consist of three bands at 481, 577 and 669 nm due to $^4F_{9/2} \rightarrow {}^6H_{15/2}$, $^4F_{9/2} \rightarrow {}^6H_{13/2}$ and $^4F_{9/2} \rightarrow {}^6H_{9/2}$ transitions, respectively (Fig. 5c). The emission bands at 481 nm and 577 nm arise from MDT and EDT of Dy^{3+}, respectively. When Dy^{3+} ions are situated at sites with relatively low symmetry, the yellow EDT band at 577 nm is dominant. When the blue MDT band at 481 nm is intense, Dy^{3+} ions occupy symmetric sites. The yellow emission is more intense than the blue emission from the LHOD NPs, which suggests the lack of inversion symmetry around Dy^{3+} in these NPs.

The Commission International del'Eclairage (CIE) chromaticity coordinates of our LHOE, LHOT and LHOD NPs were calculated from the PL emission spectra (Fig. 5d). Red, green and bluish-green emissions are clearly seen from the LHOE, LHOT and LHOD NPs, respectively, which is consistent with the digital images from the nanosized LHOE and LHOT powders under NUV excitations as shown as the insets of Fig. 5a and b.

3.4.3. Concentration quenching study

The LHOE, LHOT and LHOD NPs have similar PL emission profiles relevant to the Eu^{3+}, Tb^{3+} and Dy^{3+} dopants, however, their relative emission intensity depends on the doping concentration (Fig. 6a). For the LHOE NPs, the red emission at 612 nm ($^5D_0 \rightarrow {}^7F_2$) increases as the Eu^{3+} concentration increases initially from 0.1 to 5.0 mol% and decreases afterwards due to concentration quenching. At high doping level, neighboring Eu^{3+} ions are close to each other which leads to cross-relaxation process between them. Thus, the optimum Eu^{3+} concentration in the LHO host is 5.0 mol%. For the LHOT and LHOD NPs, concentration quenching happens at 2.5 mol% and 1.0 mol %, respectively. This phenomenon can be related to different critical distance values for these three series of NPs.

To get insight on the exact mechanisms responsible for the quenching mechanism of the LHOE, LHOT and LHOD NPs, the following equation is used to estimate their critical distances (r_c):

$$r_c = 2\left(\frac{3V}{4\pi X_c N}\right)^{\frac{1}{3}} \quad (1)$$

where r_c is the critical distance between dopant ions and quenching sites, V is unit cell volume, X_c is the critical concentration of dopant ions, and N is the number of sites that activator ions can occupy in the host. The critical distances calculated for the LHOE, LHOT, and LHOD NPs based on the above formula are 14.4 Å, 30.9 Å, and 24.6 Å, respectively. There is an reverse relation between the critical concentration and critical distance values for the LHOE, LHOT and LHOD NPs (Fig. 6b).

There are two main mechanisms for concentration quenching: exchange interaction (r_c < 5 Å) and multipolar interaction (r_c > 5 Å) [63]. The critical distances for these three series of NPs are much larger than the typical critical distance of exchange interaction, so it could be concluded that electric multipolar interactions is the main mechanism

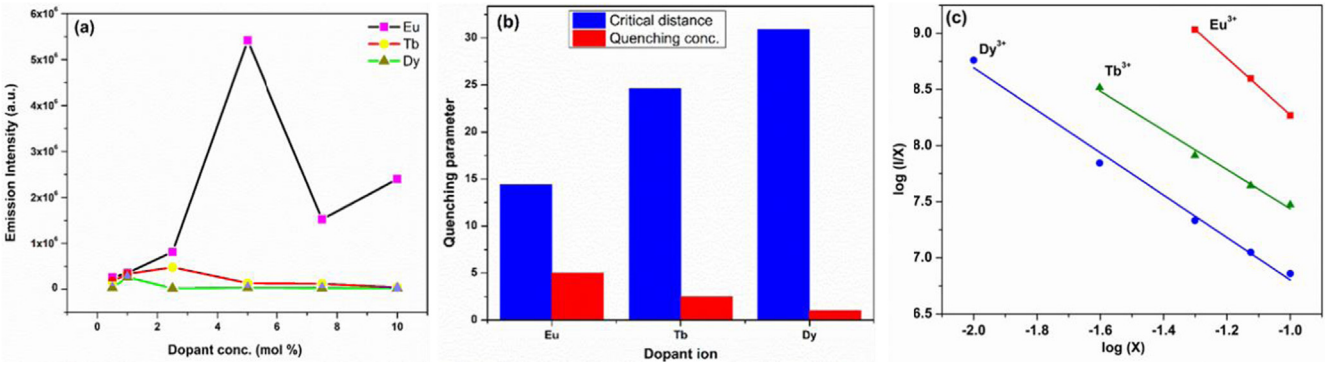

Fig. 6. (a) Variation of integrated PL emission intensity with doping concentration based on the most intense peaks of Eu, Tb and Dy dopants at 612, 543 and 577 nm, respectively, (b) comparison of critical concentration and critical distance, and (c) relation between $\log_{10}(I/x)$ and $\log_{10}(x)$ of the LHOE, LHOT and LHOD NPs.

responsible for the energy transfer from one dopant ion to another. To decipher the exact type of electric multipolar interaction responsible for non-radiative energy transfer between dopant ions in the LHOE, LHOT and LHOD NPs, we used the Van Uitert formula based on the variation of PL emission intensity per unit concentration with the energy transfer involving same acceptor and donor [64]:

$$I/x = K[1 + \beta(x)\theta/3]^{-1} \quad (2)$$

where x is the concentration of dopant ions which is not less than the critical concentration, I/x is the emission intensity I per phosphor dopant x, K and β are constants for the same excitation condition for a given phosphor, and θ value indicates the type of electric multipolar character responsible for concentration quenching. When $\theta = 3$, non-radiative energy transfer proceed via exchange interaction, while $\theta = 6$ corresponds to dipole–dipole interaction, $\theta = 8$ corresponds to dipole–quadrupole interaction, and $\theta = 10$ corresponds to quadrupole–quadrupole interaction [65]. Applying the condition of $\beta(x)\theta/3 \gg 1$, Eq. (2) is simplified into:

$$\log(I/x) = K' - \theta/3\log x (K' = \log K - \log\beta) \quad (3)$$

By plotting $\log(I/x)$ with $\log(x)$, the slope of Eq. (3) gives the value of electric multipolar character θ. For the LHOE, LHOT and LHOD NPs, the slope values as $(-\theta/3)$ of the LHOE, LHOT and LHOD NPs are -2.53504, -1.74559 and -1.73756, respectively (Fig. 6c). Therefore, the θ values are ~8, 6, and 6 for the LHOE, LHOT and LHOD NPs corresponding to the energy transfer mechanism of the LHOE NPs via a dipole − quadrupole interaction whereas those of the LHOT and LHOD NPs via a dipole–dipole interaction.

The QY values of the three best singly-doped phosphors, i.e. LHOE:5%, LHOT:2.5%, and LHOD:1.0%, are 16.88, 11.05 and 12.46, respectively.

3.4.4. Luminescence lifetime spectroscopy

The PL decay profiles of the LHOE NPs (Fig. 7a) exhibit biexponential behavior with Eu^{3+} doping concentration > 1.0%, which can be fitted into an approximate function of

$$I = I_0 + B_1\exp(-t/\tau_1) + B_2\exp(-t/\tau_2) \quad (4)$$

where I_0 is the initial emission intensity at time $t = 0$, and τ_1 and τ_2 are the short and long lifetime values. At Eu^{3+} doping concentration < 1.0%, the PL decay curve shows monoexponential behavior. This indicates homogenous distribution of Eu^{3+} ions in the LHO host at low doping level.

It is possible that at low doping concentration, Eu^{3+} ions are specifically localized only at asymmetric LaO_8 scalenohedra. At Eu^{3+} doping concentration higher than 1.0%, minor fraction (22–27%) of Eu^{3+} ions tunnel to relatively symmetric HfO_6 octahedra of LHO host. The short lifetime component corresponds to the Eu^{3+} ions surrounding with more defect states and the long lifetime component corresponds to Eu^{3+} ions surrounding with less defect states [66]. The stabilization of Eu^{3+} ions at La^{3+} sites does not invoke the need for charge compensating defects whereas that of Eu^{3+} ions at Hf^{4+} sites needs to be compensated by oxygen vacancies. When trivalent Eu^{3+} ions occupy tetravalent hafnium sites, charge compensation takes place by formation of oxygen vacancies: $2Eu^{\bullet\bullet\bullet} + 3Hf_{Hf}^{\bullet\bullet\bullet\bullet} \leftrightarrow 2Eu_{Hf}^{'} + V_O^{\bullet\bullet}$. Therefore, the short lifetime (0.94–1.19 ms) is attributed to Eu^{3+} sitting at Hf^{4+} site whereas the one at La^{3+} is having long lifetime (3.10–3.79 ms). There is no regular trend of the τ_1 and τ_2 values for the LHOE NPs as a function of Eu^{3+} doping concentration (Table 3).

The luminescence decay profiles of the LHOT NPs (Fig. 7b) yield only single lifetime in the range of 0.15 ms to 2.11 ms. Based on the PL emission spectra of the LHOT NPs discussed earlier (Fig. 5b), Tb^{3+} ions are stabilized mostly at symmetric Hf^{4+} sites in the LHO host. Such short lifetime value is due to the presence of oxygen vacancies as a

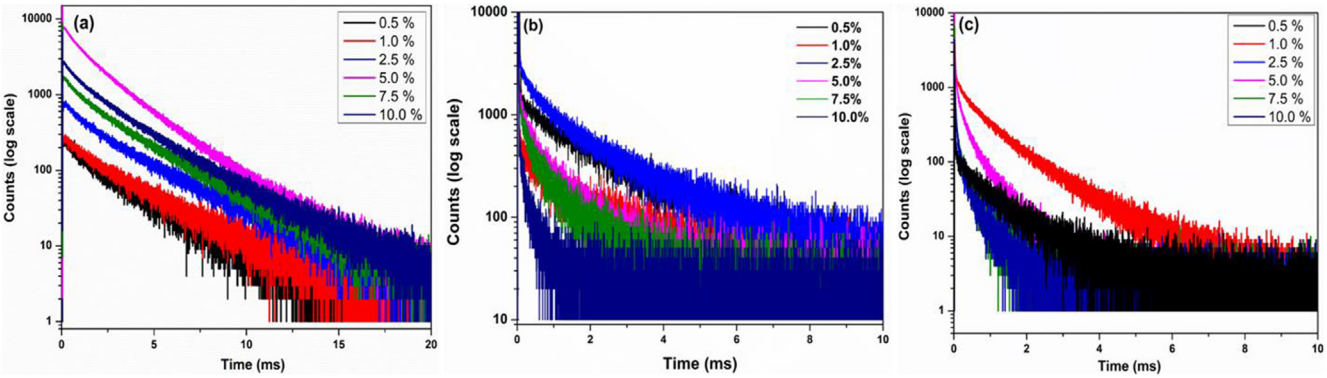

Fig. 7. PL decay profiles of the (a) LHOE (λ_{ex} = 393 nm and λ_{em} = 612 nm), (b) LHOT (λ_{ex} = 285 nm and λ_{em} = 543 nm), and (c) LHOD (λ_{ex} = 351 nm and λ_{em} = 577 nm) NPs.

Table 3
Calculated PL lifetime values of the LHOE, LHOT, and LHOD NPs.

x	τ_1 (ms)	τ_2 (ms)
$La_2Hf_2O_7$:x%Eu^{3+}		
0.5	2.63	–
1.0	3.01	–
2.5	1.19 (23%)	3.79 (77%)
5.0	0.94 (27%)	2.57 (73%)
7.5	1.03 (22%)	3.26 (78%)
10.0	0.97 (22%)	3.10 (78%)
$La_2Hf_2O_7$:x%Tb^{3+}		
0.5	2.11	–
1.0	1.49	–
2.5	1.41	–
5.0	0.76	–
7.5	0.67	–
10.0	0.15	–
$La_2Hf_2O_7$:x%Dy^{3+}		
0.5	1.042	–
1.0	0.34 (24%)	1.34 (76%)
2.5	0.11 (34%)	0.82 (66%)
5.0	0.094 (37%)	0.64 (63%)
7.5	0.024 (38%)	0.345 (62%)
10.0	0.019 (42%)	0.323 (58%)

charge compensating defects that provide non-radiative pathways. Also, the lifetime value monotonically decreases with increasing Tb^{3+} concentration, which can be attributed to increasing non-radiative relaxation rate due to the cross-relaxation processes among Tb^{3+} ions.

The decay profiles of the LHOD NPs exhibit monoexponential behavior when the Dy^{3+} doping level is smaller than 0.5% and biexponential decay afterwards (Fig. 7c). For the latter case, the fast component (0.019–0.34 ms) corresponds to the Dy^{3+} ions occupying Hf^{4+} site and the slow component (0.32–1.34 ms) corresponds to the Dy^{3+} localized at La^{3+} site. The population of the fast component gradually increases from 24 to 42% with increasing Dy^{3+} concentration from 1.0% to 10.0% in the LHOD NPs. Similar to the LHOT NPs, both the fast and slow decay components decrease as the Dy^{3+} doping concentration increases due to the cross-relaxation processes among Dy^{3+} ions.

3.5. RL

The light output of the nanoparticles under X-ray irradiation is another important characteristic to understand its RL properties. $La_2Hf_2O_7$ is a dense and high-Z material, which has high probability of absorbing X-ray through photoelectric effect. Unlike fluorescence, which is single molecule property, scintillation is governed by bulk property of materials [44]. The XEOL spectra of the LHOE, LHOT and LHOD NPs (Fig. 8a, b and c) display intense red, green and yellow emission bands corresponding to $^5D_0 \rightarrow {}^7F_2$, $^5D_4 \rightarrow {}^7F_5$ and $^4F_{9/2} \rightarrow {}^6H_{13/2}$ transitions of Eu^{3+}, Tb^{3+} and Dy^{3+}, respectively. The concentration dependence of the XEOL spectra is in agreement with their PL spectra (Fig. 6). The schematic showing red, green and yellow color emissions from the LHOE, LHOT and LHOD NPs under X-ray excitation is shown in Fig. 8d. To the best of our knowledge, this is the first report of green and yellow RL emissions from Tb^{3+} and Dy^{3+} doped LHO NPs. With

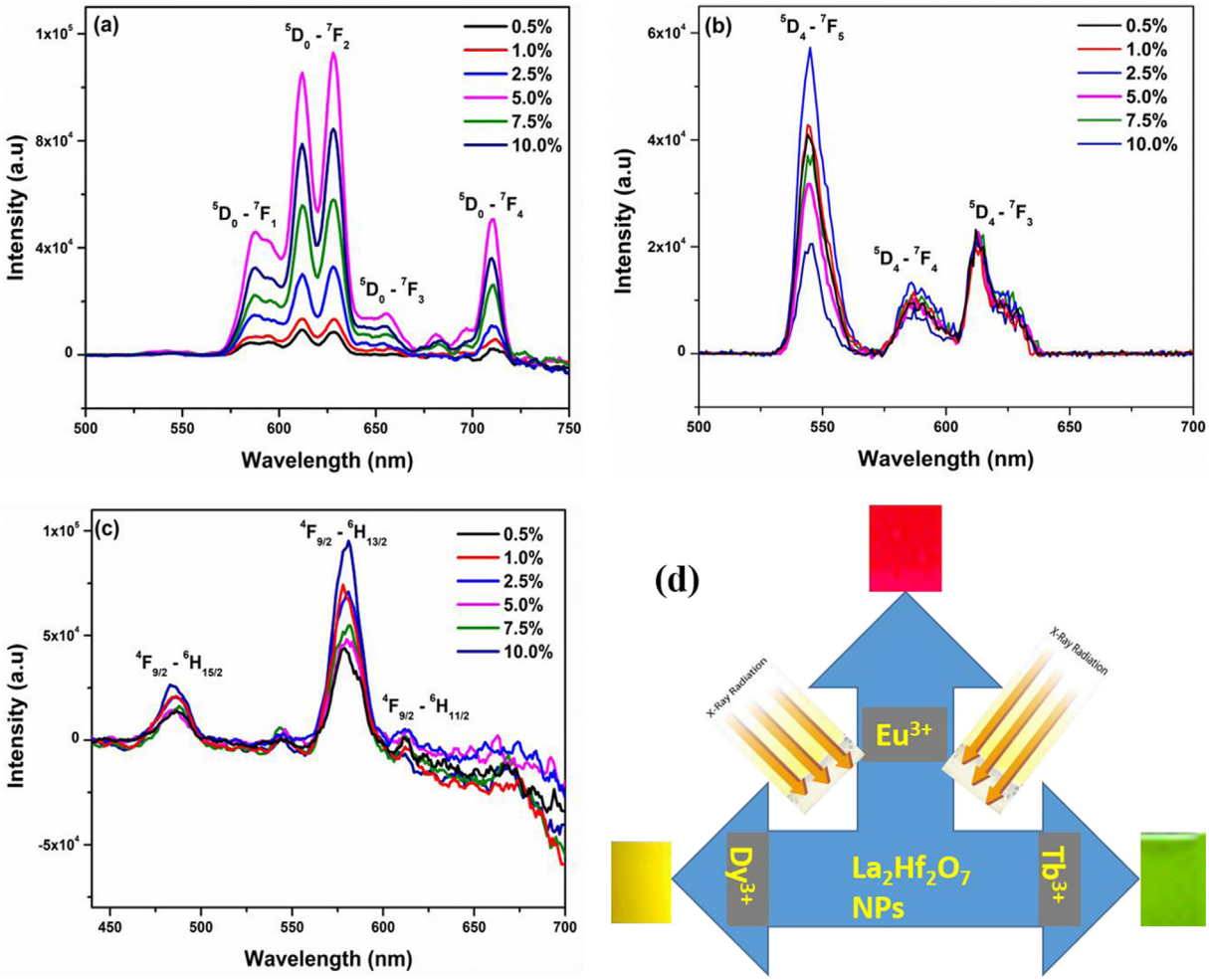

Fig. 8. RL emission spectra of the (a) LHOE, (b) LHOT, and (c) LHOD NPs. (d) Schematic diagram depicting RL emission from the LHOE-5.0%, LHOT-2.5%, and LHOD-1.0% NPs.

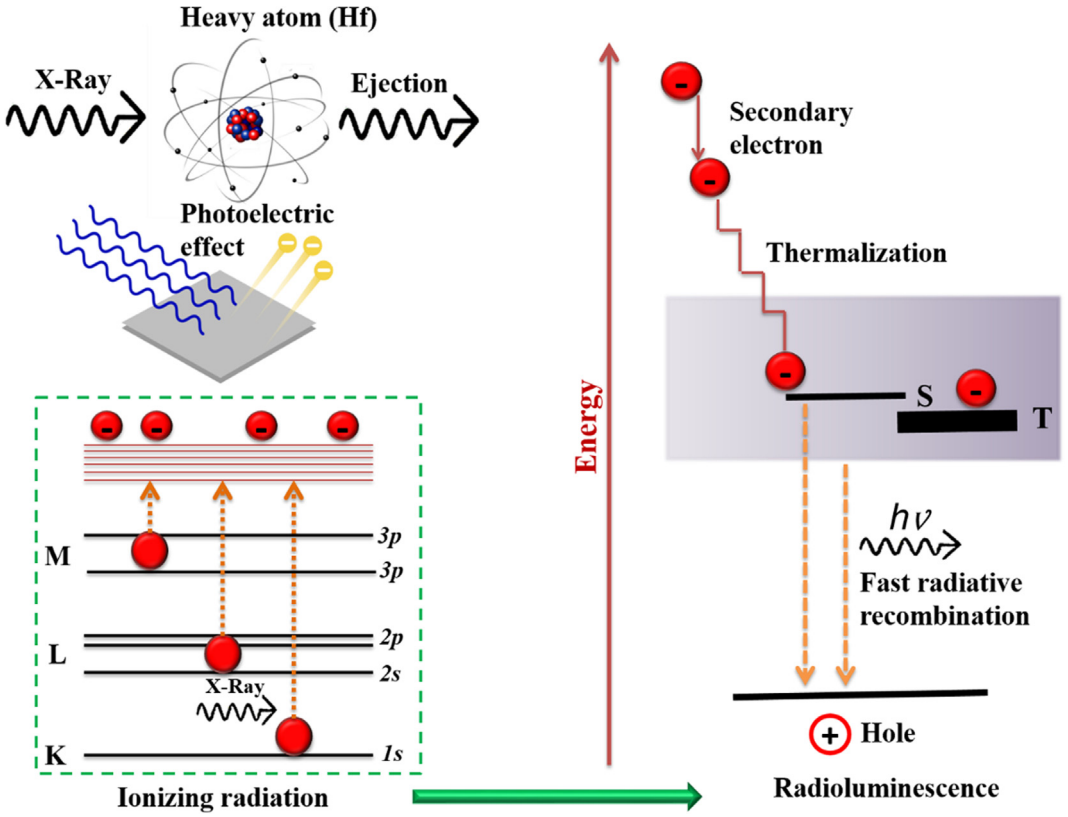

Fig. 9. Proposed mechanism of X-ray scintillation in RE doped LHO NPs.

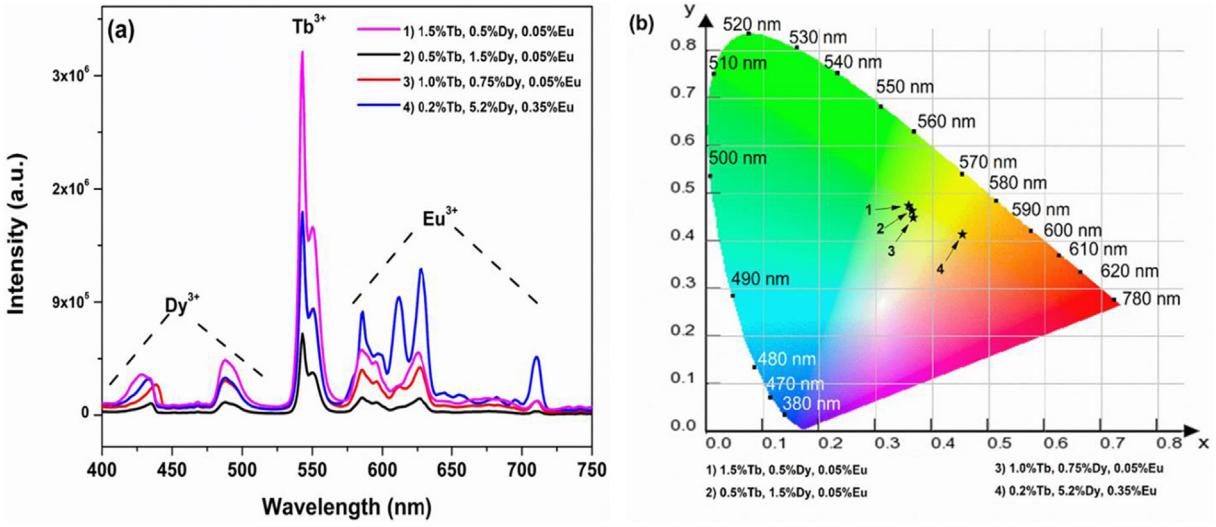

Fig. 10. (a) Emission spectra and (b) CIE index diagram of the triply-doped $La_2Hf_2O_7:Eu^{3+},Tb^{3+},Dy^{3+}$ NPs under 254 nm excitation. The chemical composition corresponding to the data points is given in Table 4.

Table 4
Color coordinates and color temperature of the triply-doped $La_2Hf_2O_7:Eu^{3+},Tb^{3+},Dy^{3+}$ NPs under 254 nm excitation.

Triply co-doped system	CIE index	CCT
(1) 1.5%Tb, 0.5 %Dy, 0.05%Eu	(0.357, 0.475)	4930
(2) 0.5%Tb, 1.5%Dy, 0.05%Eu	(0.363, 0.465)	4780
(3) 1.0%Tb, 0.75%Dy, 0.05%Eu	(0.366, 0.450)	4690
(4) 0.2%Tb, 5.25%Dy, 0.35%Eu	(0.415, 0.526)	2830

the exciting preliminary RL results from these NPs, we plan to make transparent ceramics out of them for desirable scintillation properties for applications in the areas of radiation detection, bioimaging, nuclear safety, security, etc [67].

RL emission on X-ray irradiation takes place after various processes that initiates once large quantity of electron is created in conduction bands (CB) and holes in the valence bands (VB). Fig. 9 presents a probable mechanism for the observed RL in the pyrochlore NPs. The mechanism of intense X-ray scintillation could be attributed in part to the strong X-ray stopping power of LHO NPs due to heavy Hf atom.

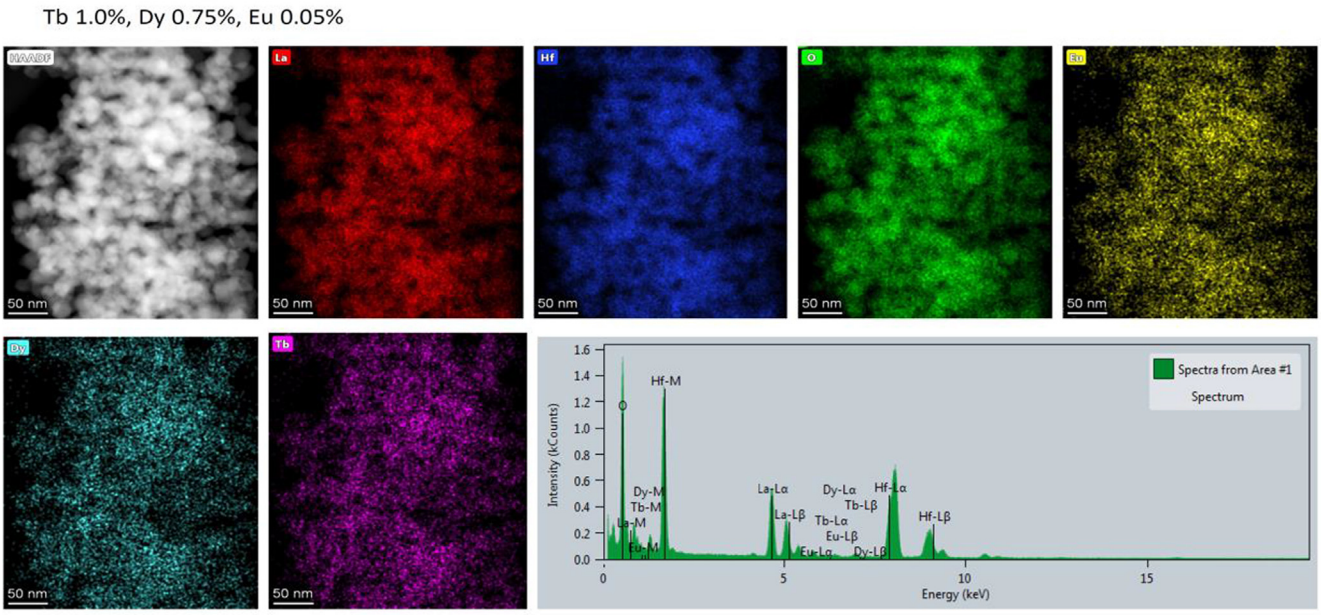

Fig. 11. HAADF image, elemental mappings and EDS spectrum of the representative LHO:1.0%Tb,0.75%Dy,0.05%Eu NPs.

3.6. Warm white light emission from the triply-doped LHO NPs

As discussed above, the LHOE-5.0%, LHOT-2.5%, and LHOD-1.0% NPs emit red, green and blue light (Fig. 5d). Based on RGB mixing strategy and with the aim to generate warm white light, the LHO host is triply-doped with these three activators of Eu^{3+}, Tb^{3+}, and Dy^{3+}. Optimization of the doping concentration of these three ions was based on the results gathered from the emission spectra of the singly doped LHOE, LHOT, and LHOD NPs. Concentration quenching from these singly doped systems was considered to narrow down the doping range and applied to our triply-doped LHO NPs development for warm white light generation. Specifically, the Tb^{3+} concentration decreased from 1.5% to 0.2%, but the Dy^{3+} and Eu^{3+} concentrations are raised from 0.5% to 5.25% and 0.05% to 0.35%, respectively (Fig. 10).

Color coordinates and correlated color temperature (CCT) are important parameters to determine phosphor performance. While optimizing triply-doping of the LHO NPs, the CIE color of the LHO:Eu,Tb,Dy nanophosphors shifted from greenish white to warm white light (yellowish white) (Fig. 10b). Correspondingly, the CCT of the generated white light was tuned from 4930 to 2830 K (Table 4). The LHO:0.2%Tb,5.25%Dy,0.35%Eu NPs displayed perfect warm white light with a low CCT value of 2830 K. The QY of this particular triply doped nanoparticulate sample is found to be 8.11%, which is low compared to the commercial phosphors. Considering the advantages of the LHO pyrochlore host such as high thermal stability, structural stability and low phonon energy, we intend to improve its QY with improving design strategies such as core–shell strategy, co-doping charge compensator and tuning the doping concentration. Based on the exciting results, we are developing LEDs using these NPs and performing electroluminescence measurements. The obtained results will be published separately in near future.

Formation of nanoparticles in case of the triply co-doped LHO samples is also confirmed using high-angle annular dark-field imaging (Fig. 11, top left figure). We have also carried out EDS measurements on one of the representative triply-doped LHO samples to show our efficient method for preparing triply co-doped Eu, Dy, Tb LHO NPs and the obtained atomic fractions of the co-doped samples are within the limit of error. Elemental mapping (Fig. 11) clearly shows uniform distribution of the dopants and the matrix ions. The representative EDS spectrum shows the presence of X-ray lines of Eu, Tb and Dy ions along with those of La, Hf and O ions. We have worked on the actual dopant concentrations of the LHO:1.0%Tb,0.75%Dy,0.05%Eu sample with EDS. Given the close overlap of the three dopant peaks, it is worth noting that the relative quantities of the dopants measured for the co-doped samples are not accurate.

4. Conclusion

In summary, we explored the luminescence properties of pyrochlore $La_2Hf_2O_7$ nanoparticles which were singly and triply doped with Eu^{3+}, Tb^{3+} and Dy^{3+}. The singly doped LHO NPs with Eu^{3+}, Tb^{3+} and Dy^{3+} displayed red, green and yellowish-blue emission under near ultraviolet irradiation, respectively. The non-radiative energy transfer mechanism of the Tb^{3+} and Dy^{3+} doped LHO NPs is a dipole−dipole interaction whereas that of the Eu^{3+} doped LHO NPs is a dipole-quadrupole interaction causing concentration quenching. Lifetime spectroscopy suggests concentration dependent site swapping in the Eu^{3+} and Dy^{3+} doped LHO NPs whereas Hf^{4+} is specifically occupied site in the Tb^{3+} doped LHO NPs. Moreover, triply-doped $La_2Hf_2O_7$:Eu^{3+},Tb^{3+},Dy^{3+} NPs exhibit warm white luminescence with low CCT which is highly beneficial for indoor lighting. By optimizing dopant concentration, the emission color of the triply-doped NPs can be adjusted from greenish white to yellowish white and the correlated color temperature can be lowered. The tunable luminescence properties of these doped lanthanum hafnate NPs indicate their great application potentials in solid-state lighting and multicolor luminescence devices.

Acknowledgement

The authors thank the financial support by the National Science Foundation under CHE (award #1710160, YM), DMR (CAREER award #1455154, BG and MG), and EPSCoR (#1355438, MT). SKG thanks the United States-India Education Foundation (USIEF, India) and the Institute of International Education (IIE, USA) for his Fulbright Nehru Postdoctoral Fellowship (Award# 2268/FNPDR/2017). This work was performed in part at the EMC which belongs to the National Science Foundation NNCI Kentucky Multiscale Manufacturing and Nano Integration Node, supported by ECCS-1542174.

References

[1] P. Pust, V. Weiler, C. Hecht, A. Tücks, A.S. Wochnik, A.-K. Henß, D. Wiechert, C. Scheu, P.J. Schmidt, W. Schnick, Narrow-band red-emitting $Sr[LiAl_3N_4]:Eu^{2+}$ as a next-generation LED-phosphor material, Nat. Mater. 13 (2014) 891.

[2] P. Pust, P.J. Schmidt, W. Schnick, A revolution in lighting, Nat. Mater. 14 (5) (2015) 454.

[3] C. Maak, P. Strobel, V. Weiler, P.J. Schmidt, W. Schnick, Unprecedented Deep-Red Ce^{3+} Luminescence of the Nitridolithosilicates $Li_{38.7}RE_{3.3}Ca_{5.7}[Li_2Si_{30}N_{59}]O_2F$ (RE = La, Ce, Y), Chem. Mater. 30 (15) (2018) 5500–5506.

[4] M. Zhao, H. Liao, L. Ning, Q. Zhang, Q. Liu, Z. Xia, Next-Generation Narrow-Band Green-Emitting $RbLi(Li_3SiO_4)_2:Eu^{2+}$ Phosphor for Backlight Display Application, Adv. Mater. 30 (38) (2018) 1802489.

[5] M. Pan, W.-M. Liao, S.-Y. Yin, S.-S. Sun, C.-Y. Su, Single-Phase White-Light-Emitting and Photoluminescent Color-Tuning Coordination Assemblies, Chem. Rev. 118 (18) (2018) 8889–8935.

[6] Q. Wang, D. Ma, Management of charges and excitons for high-performance white organic light-emitting diodes, Chem. Soc. Rev. 39 (7) (2010) 2387–2398.

[7] H. Wu, L. Ying, W. Yang, Y. Cao, Progress and perspective of polymer white light-emitting devices and materials, Chem. Soc. Rev. 38 (12) (2009) 3391–3400.

[8] K.T. Kamtekar, A.P. Monkman, M.R. Bryce, Recent Advances in White Organic Light-Emitting Materials and Devices (WOLEDs), Adv. Mater. 22 (5) (2010) 572–582.

[9] M. Jacoby, The chemical search for better white light, Chem. Eng. News 96 (2019) 46.

[10] S.K. Gupta, K. Sudarshan, R.M. Kadam, Tunable white light emitting $Sr_2V_2O_7:Bi^{3+}$ phosphors: role of bismuth ion, Mater. Des. 130 (2017) 208–214.

[11] P. Li, Z. Wang, Z. Yang, Q. Guo, A novel, warm, white light-emitting phosphor $Ca_2PO_4Cl:Eu^{2+}$, Mn^{2+} for white LEDs, J. Mater. Chem. C 2 (2014) 7823–7829.

[12] Z. Wang, P. Li, Q. Guo, Z. Yang, A single-phased warm white-light-emitting phosphor $BaMg_2(PO_4)_2:Eu^{2+}$, Mn^{2+}, Tb^{3+} for white light emitting diodes, Mater. Res. Bull. 52 (2014) 30–36.

[13] N. Guo, Y. Zheng, Y. Jia, H. Qiao, H. You, Warm-White-Emitting from Eu^{2+}/Mn^{2+}-Codoped $Sr_3Lu(PO_4)_3$ Phosphor with Tunable Color Tone and Correlated Color Temperature, J. Phys. Chem. C 116 (2012) 1329–1334.

[14] J. Adam, W. Metzger, M. Koch, P. Rogin, T. Coenen, J.S. Atchison, P. König, Light emission intensities of luminescent Y_2O_3:Eu and Gd_2O_3:Eu particles of various sizes, Nanomaterials 7 (2) (2017) 26.

[15] H. Luitel, A Novel Orange-Red Emitting $ZnB_4O_7:Eu^{3+}$ Phosphor with Urchin like, Nanostructure (2015).

[16] S.K. Rao, P. Indira, K. Murthy, Rare earth doped $LaPO_4$ phosphor synthesis and characterization, Int. J. Sci. Eng. 4 (2013) 1032–1039.

[17] Q. Liang, C. Han, C. Duan, H. Xu, Blue Thermally Activated Delayed Fluorescence-Emitting Phosphine Oxide Hosts for Ultrasimple and Highly Efficient White Organic Light-Emitting Diodes, Adv. Opt. Mater. 6 (12) (2018) 1800020.

[18] E. Sreeja, V. Vidyadharan, S.K. Jose, A. George, C. Joseph, N.V. Unnikrishnan, P.R. Biju, A single-phase white light emitting Pr^{3+} doped Ba_2CaWO_6 phosphor: synthesis, photoluminescence and optical properties, Opt. Mater. 78 (2018) 52–62.

[19] C.N. Pangul, S.W. Anwane, S.B. Kondawar, Enhanced photoluminescence properties of electrospun Dy^{3+}-doped ZnO nanofibres for white lighting devices, Luminescence 33 (6) (2018) 1087–1093.

[20] H. Xu, L. Wang, L. Tan, D. Wang, C. Wang, J. Shi, Sites occupancy preference of Bi^{3+} and white light emission through co-doped Sm^{3+} in $LiGd_5P_2O_8$, J. Am. Ceram. Soc. 101 (8) (2018) 3414–3423.

[21] J. Zhong, X. Chen, D. Chen, M. Liu, Y. Zhu, X. Li, Z. Ji, A novel rare-earth free red-emitting $Li_3Mg_2SbO_6:Mn^{4+}$ phosphor-in-glass for warm w-LEDs: Synthesis, structure, and luminescence properties, J. Alloy. Compd. 773 (2019) 413–422.

[22] H. Patnam, S.K. Hussain, L.K. Bharat, J.S. Yu, Near-ultraviolet excited Tm^{3+} and Dy^{3+} ions co-doped barium lanthanum silica oxide phosphors for white-light applications, J. Alloy. Compd. 780 (2019) 846–855.

[23] J.P. Zuniga, S.K. Gupta, M. Pokhrel, Y. Mao, Exploring the optical properties of $La_2Hf_2O_7:Pr^{3+}$ nanoparticles under UV and X-ray excitation for potential lighting and scintillating applications, New J. Chem. 42 (2018) 9381–9392.

[24] J.P. Zuniga, S.K. Gupta, M. Abdou, Y. Mao, Effect of molten salt synthesis processing duration on the photo- and radioluminescence of UV-, Visible-, and X-ray-excitable $La_2Hf_2O_7:Eu^{3+}$ nanoparticles, ACS Omega 3 (2018) 7757–7770.

[25] H. Gupta, S. Brown, N. Rani, V. Gohel, A lattice dynamical investigation of the Raman and the infrared frequencies of the cubic $A_2Hf_2O_7$ pyrochlores, J. Phys. Chem. Solids 63 (2002) 535–538.

[26] J. Trojan-Piegza, S. Gierlotka, E. Zych, W. Lojkowski, Spectroscopic studies of nanopowder and nanoceramics $La_2Hf_2O_7$:Pr scintillator, J. Am. Ceram. Soc. 97 (2014) 1595–1601.

[27] Y.-M. Ji, D.-Y. Jiang, J.-L. Shi, Preparation and spectroscopic properties of $La_2Hf_2O_7$/Tb, Mater. Lett. 59 (8) (2005) 868–871.

[28] Y. Eagleman, M. Weber, A. Chaudhry, S. Derenzo, Luminescence study of cerium-doped $La_2Hf_2O_7$: effects due to trivalent and tetravalent cerium and oxygen vacancies, J. Lumin. 132 (2012) 2889–2896.

[29] M. Hirayama, N. Sonoyama, A. Yamada, R. Kanno, Relationship between structural characteristics and photoluminescent properties of $(La_{1-x}Eu_x)_2M_2O_7$ (M = Zr, Hf, Sn) pyrochlores, J. Lumin 128 (2008) 1819–1825.

[30] S.K. Gupta, V. Grover, R. Shukla, K. Srinivasu, V. Natarajan, A.K. Tyagi, Exploring pure and RE co-doped (Eu^{3+}, Tb^{3+} and Dy^{3+}) gadolinium scandate: luminescence behaviour and dynamics of energy transfer, Chem. Eng. J 283 (2016) 114–126.

[31] K. Das, A. Marathe, X. Zhang, Z. Zhao, J. Chaudhuri, Superior white light emission and color tunability of tri-doped $YBO_3:Tb^{3+}$, Eu^{3+} and Dy^{3+} for white light emitting diodes, RSC Adv. 6 (97) (2016) 95055–95061.

[32] Y. Liu, G. Liu, J. Wang, X. Dong, W. Yu, Single-Component and Warm-White-Emitting Phosphor $NaGd(WO_4)_2:Tm^{3+}$, Dy^{3+}, Eu^{3+}: Synthesis Luminescence, Energy Transfer, and Tunable Color, Inorganic Chem. 53 (21) (2014) 11457–11466.

[33] N.S. Singh, N.K. Sahu, D. Bahadur, Multicolor tuning and white light emission from lanthanide doped $YPVO_4$ nanorods: energy transfer studies, J. Mater. Chem. C 2 (3) (2014) 548–555.

[34] R.S. Rejith, J.K. Thomas, S. Solomon, Structural, optical and impedance spectroscopic characterizations of $RE_2Zr_2O_7$ (RE = La, Y) ceramics, Solid State Ion. 323 (2018) 112–122.

[35] G.M. Mustafa, S. Atiq, S.K. Abbas, S. Riaz, S. Naseem, Tunable structural and electrical impedance properties of pyrochlores based Nd doped lanthanum zirconate nanoparticles for capacitive applications, Ceram. Int. 44 (2) (2018) 2170–2177.

[36] A. Jamil, J. Schläfer, Y. Gönüllü, A. Lepcha, S. Mathur, Precursor-derived rare earth metal pyrochlores: $Nd_2Sn_2O_7$ nanofibers and thin films as efficient photoabsorbers, Cryst. Growth. Des. 16 (2016) 5260–5267.

[37] S. Zinatloo-Ajabshir, Z. Salehi, M. Salavati-Niasari, Green synthesis and characterization of $Dy_2Ce_2O_7$ nanostructures using Ananas comosus with high visible-light photocatalytic activity of organic contaminants, J. Alloys Compd. 763 (2018) 314–321.

[38] M.G. Nikolic, M.S. Rabasovic, J. Krizan, S. Savic-Sevic, M.D. Rabasovic, B.P. Marinkovic, A. Vlasic, D. Sevic, Luminescence thermometry using $Gd_2Zr_2O_7:Eu^{3+}$, Opt. Quant. Elctron. 50 (6) (2018) 258.

[39] R. Zhu, J. Zou, D. Wang, K. Zou, D. Gao, J. Mao, M. Liu, X-ray diffractional, spectroscopic and thermo-physical properties analyses on Eu-doped lanthanum zirconate ceramic for thermal barrier coatings, J. Alloys Compd. 746 (2018) 62–67.

[40] M. Pokhrel, K. Wahid, Y. Mao, Systematic studies on $RE_2Hf_2O_7$:5%Eu^{3+} (RE = Y, La, Pr, Gd, Er, and Lu) nanoparticles: effects of the A-site RE^{3+} cation and calcination on structure and photoluminescence, J. Phys. Chem. C 120 (27) (2016) 14828–14839.

[41] M. Abdou, S.K. Gupta, J.P. Zuniga, Y. Mao, On structure and phase transformation of uranium doped $La_2Hf_2O_7$ nanoparticles as an efficient nuclear waste host, Mater. Chem. Front. 2 (2018) 2201–2211.

[42] X. Chen, Y. Liu, D. Tu, Lanthanide-doped luminescent nanomaterials, Springer, 2016.

[43] S.K. Gupta, M. Mohapatra, V. Natarajan, S.V. Godbole, Site-specific luminescence of Eu^{3+} in gel-combustion-derived strontium zirconate perovskite nanophosphors, J. Mater. Sci. 47 (8) (2012) 3504–3515.

[44] J.S. Klein, C. Sun, G. Pratx, Radioluminescence in biomedicine: physics, applications, and models, Phys. Med. Biol. 64(4) (2019) 04TR01.

[45] S.K. Gupta, J.P. Zuniga, M. Abdou, Y. Mao, Thermal annealing effects on $La_2Hf_2O_7:Eu^{3+}$ nanoparticles: a curious case study of structural evolution and site-specific photo- and radio-luminescence, Inorg. Chem. Front. 5 (2018) 2508–2521.

[46] S.K. Gupta, J.P. Zuniga, P.S. Ghosh, M. Abdou, Y. Mao, Correlating Structure and Luminescence Properties of Undoped and $La_2Hf_2O_7:Eu^{3+}$ NPs Prepared with Different Coprecipitating pH Values through experimental and theoretical studies, Inorg. Chem. 57 (2018) 11815–11830.

[47] J.P. Zuniga, M. Abdou, S.K. Gupta, Y. Mao, Molten-Salt Synthesis of Complex Metal Oxide Nanoparticles, JoVE, e58482.

[48] M. Pokhrel, S.K. Gupta, K. Wahid, Y. Mao, Pyrochlore Rare-Earth Hafnate $RE_2Hf_2O_7$ (RE = La and Pr) Nanoparticles Stabilized by Molten-Salt Synthesis at Low Temperature, Inorg. Chem. 58 (2019) 1241–1251.

[49] E. Gilardi, E. Fabbri, L. Bi, J.L.M. Rupp, T. Lippert, D. Pergolesi, E. Traversa, Effect of Dopant-Host Ionic Radii Mismatch on Acceptor-Doped Barium Zirconate Microstructure and Proton Conductivity, J. Phys. Chem. C 121 (2017) 9739–9747.

[50] R.D. Shannon, Revised effective ionic radii and systematic studies of interatomic distances in halides and chalcogenides, Acta crystallographica section A: crystal physics, diffraction, theoretical and general crystallography 32 (5) (1976) 751–767.

[51] Y. Gao, Y. Sun, H. Zou, Y. Sheng, X. Zhou, B. Zhang, B. Zhou, Effect of Eu^{3+} doping on the structural and photoluminescence properties of cubic $CaCO_3$, Mater. Sci. Eng. B 203 (2016) 52–58.

[52] B. Paul, K. Singh, T. Jaroń, A. Roy, A. Chowdhury, Structural properties and the fluorite–pyrochlore phase transition in $La_2Zr_2O_7$: the role of oxygen to induce local disordered states, J. Alloys Compd. 686 (2016) 130–136.

[53] S. Gu, S. Zhang, B. Xue, J. Yan, W. Li, L. Zhang, Phase variation and thermophysical properties of $La_2Hf_2O_7$ with alumina addition, J. Eur. Ceram. Soc. 38 (2018) 1938–1945.

[54] M. Pokhrel, S.K. Gupta, K. Wahid, Y. Mao, Pyrochlore Rare-Earth Hafnate $RE_2Hf_2O_7$ (RE = La and Pr) Nanoparticles Stabilized by Molten-Salt Synthesis at Low Temperature, Inorg. Chem. (2019).

[55] N. Garg, K.K. Pandey, C. Murli, K.V. Shanavas, B.P. Mandal, A.K. Tyagi, S.M. Sharma, Decomposition of lanthanum hafnate at high pressures, Phys. Rev. B 77 (2008) 214105.

[56] S.A. Kumar, J. Senthilselvan, Effect of calcination temperatures on Green luminescence of Ce:YAG nanophosphor prepared by modified co-precipitation method, AIP Conference Proceedings, AIP Publishing (2017) 050112.

[57] P.C. Ricci, C.M. Carbonaro, R. Corpino, C. Cannas, M. Salis, Optical and Structural Characterization of Terbium-Doped Y_2SiO_5 Phosphor Particles, J. Phys. Chem. C 115 (2011) 16630–16636.

[58] A. Potdevin, G. Chadeyron, V. Briois, F. Leroux, R. Mahiou, Modifications involved by acetylacetone in properties of sol–gel derived $Y_3Al_5O_{12}:Tb^{3+}$ – II: optical features, Dalton Trans. 39 (2010) 8718–8724.

[59] S. Chemingui, M. Ferhi, K. Horchani-Naifer, M. Férid, Synthesis and luminescence characteristics of Dy^{3+} doped $KLa(PO_3)_4$, J. Lumin 166 (2015) 82–87.

[60] F.S. Richardson, Terbium(III) and europium(III) ions as luminescent probes and

stains for biomolecular systems, Chem. Rev. 82 (1982) 541–552.
[61] S.K. Gupta, P.S. Ghosh, A.K. Yadav, N. Pathak, A. Arya, S.N. Jha, D. Bhattacharyya, R.M. Kadam, Luminescence Properties of $SrZrO_3/Tb^{3+}$ Perovskite: Host-Dopant Energy-Transfer Dynamics and Local Structure of Tb^{3+}, Inorg. Chem. 55 (2016) 1728–1740.
[62] L.P. Singh, N.P. Singh, S.K. Srivastava, Terbium doped SnO_2 nanoparticles as white emitters and SnO_2:5Tb/Fe_3O_4 magnetic luminescent nanohybrids for hyperthermia application and biocompatibility with HeLa cancer cells, Dalton Trans. 44 (2015) 6457–6465.
[63] H. Guan, Y. Sheng, Y. Song, C. Xu, X. Zhou, K. Zheng, Z. Shi, H. Zou, $YF_3:RE^{3+}$ (RE = Dy, Tb, Eu) Sub-microstructures: Controllable Morphology, Tunable Multicolor, and Thermal Properties, J. Phys. Chem. C 121 (2017) 23080–23095.
[64] L. Van Uitert, Characterization of energy transfer interactions between rare earth ions, J. Electrochem. Soc. 114 (1967) 1048–1053.
[65] M. Ilhan, R. Samur, H. Demirer, F. Mindivan, Photoluminescence and concentration quenching of Pr^{3+} doped $BaTa_2O_6$ phosphor, Metalurgija 54 (2015) 407–410.
[66] Q. Dai, H. Song, M. Wang, X. Bai, B. Dong, R. Qin, X. Qu, H. Zhang, Size and Concentration Effects on the Photoluminescence of $La_2O_2S:Eu^{3+}$ Nanocrystals, J. Phys. Chem. C 112 (2008) 19399–19404.
[67] D.R. Cooper, J.A. Capobianco, J. Seuntjens, Radioluminescence studies of colloidal oleate-capped β-Na(Gd, Lu)$F_4:Ln^{3+}$ nanoparticles (Ln = Ce, Eu, Tb), Nanoscale 10 (16) (2018) 7821–7832.